Electronic Supplement of

"Composition and mixing state of atmospheric aerosols determined by electron microscopy: method development and application to aged Saharan dust deposition in the Caribbean boundary layer"

Konrad Kandler[1,*], Kilian Schneiders[1], Martin Ebert[1], Markus Hartmann[1,+], Stephan Weinbruch[1], Maria Prass[2], Christopher Pöhlker[2]

[1]Institute for Applied Geosciences, Technical University Darmstadt, 64287 Darmstadt, Germany
[2]Max Planck Institute for Chemistry, Multiphase Chemistry Department, 55128 Mainz, Germany
[+]now at: Experimental Aerosol and Cloud Microphysics Department, Tropos Leibniz-Institute für Tropospheric Research (TROPOS), 04318 Leipzig, Germany

[*]*Correspondence to:* K. Kandler (kandler@geo.tu-darmstadt.de)

S.1 Calculation of the feldspar indices

The index value showing the closeness of a particle composition to pure feldspar is based on three values, the overall contribution of feldspar-specific elements to the particle composition and the vicinities to the feldspar Al/Si ratio as well as to the K/Si or alkali/Si ratio. The overall contribution of specific elements is calculated as

$$r_{Sil}=\frac{\langle Na\rangle+\langle Al\rangle+\langle Si\rangle+\langle K\rangle+\langle Ca\rangle}{\langle Na\rangle+\langle Al\rangle+\langle Si\rangle+\langle K\rangle+\langle Ca\rangle\ +\ \langle Mg\rangle+\langle P\rangle+\langle S\rangle+\langle Cl\rangle+\langle Ti\rangle+\langle Fe\rangle} \quad (1)$$

The vicinity with respect to Al/Si is determined as

$$r_{fsp,\,Al/Si}=\frac{\langle Al\rangle}{\langle Si\rangle}\ \frac{3\langle Na\rangle+3\langle K\rangle+2\langle Ca\rangle}{\langle Na\rangle+\langle K\rangle+2\langle Ca\rangle} \quad (2)$$

$$Q_{fsp,\,Al/Si}=\begin{cases}1-\lg\left(r_{fsp,Al/Si}\right) & \forall\ 0.1\le r_{fsp,Al/Si}\le 10\\ 0 & \forall\ r_{fsp,Al/Si}<0.1\\ 0 & \forall\ r_{fsp,Al/Si}>10\end{cases} \quad (3)$$

Closeness with respect to the K and alkali ratio is calculated as

$$r_{fsp,\,K/Si}=\frac{3\langle K\rangle}{\langle Si\rangle} \quad (4)$$

$$Q_{fsp,\,Al/Si}=\begin{cases}1-\lg\left(r_{fsp,K/Si}\right) & \forall\ 0.1\le r_{fsp,K/Si}\le 10\\ 0 & \forall\ r_{fsp,K/Si}<0.1\\ 0 & \forall\ r_{fsp,K/Si}>10\end{cases} \quad (5)$$

$$r_{fsp,\,NaKCa/Si}=\frac{3\langle Na\rangle+3\langle K\rangle+2\langle Ca\rangle}{\langle Si\rangle} \quad (6)$$

$$Q_{fsp,\,Al/Si}=\begin{cases}1-\lg\left(r_{fsp,NaKCa/Si}\right) & \forall\ 0.1\le r_{fsp,NaKCa/Si}\le 10\\ 0 & \forall\ r_{fsp,NaKCa/Si}<0.1\\ 0 & \forall\ r_{fsp,NaKCa/Si}>10\end{cases} \quad (7)$$

The vicinity of a particle's composition to pure feldspar in expressed then as

$$P_{fsp}=r_{Sil}\ Q_{fsp,\,Al/Si}\ Q_{fsp,\,NaKCa/Si} \quad (8)$$

and to pure K feldspar as

$$P_{fsp,K}=r_{Sil}\ Q_{fsp,\,Al/Si}\ Q_{fsp,\,K/Si} \quad (9)$$

For example, the P_{fsp} value becomes 1 for pure albite and 0 for sodium chloride or quartz.

S.2 Estimation of the dust contribution to each single particle in a dust / sea-salt / sulfate mixture and the size of the according dust inclusion

Refer to section 2.3.4 of the main manuscript for the general procedure and reasoning of upper and lower limit calculations.

For this model step, the following assumptions are made:

1. There is exactly one dust inclusion in each mixed particle
2. Carbonaceous matter does not contribute
3. Ca contributes to dust as carbonate
4. Ca contributes to non-dust as sulfate / chloride
5. Fe contributes to dust as Fe^{3+}
6. S contributes as sulfate
7. Na, Mg, Al, Si, P, K, Ti and Fe contribute to the dust according to their oxide weights
8. N-containing compounds contribute only in case of a non-neutral ion balance as ammonium and nitrate
9. Dust density is $\rho_{dust}=2650\,\frac{kg}{m^3}$, non-dust density is $\rho_{nondust}=2200\,\frac{kg}{m^3}$, averaged from typical dust and non-dust constituents: illite, kaolinite, muscovite, quartz, albite, microcline, calcite, gypsum, halite, sodium sulfate minerals in different hydratation states, and mascagnite (Deer et al. 1992; Warneck et al. 2012)

Estimation of the upper limit

Following the above-listed assumptions, the apparent cation/anion charge ratio is defined as

$$r_{cat}=\frac{\sum \text{cations}_{charge}}{\sum \text{anions}_{charge}} \quad (10)$$

with $\sum \text{cations}_{charge}=|Na|+2|Mg|+|K|+2|Ca|$, apparent sum of cation charges,

and $\sum \text{anions}_{\text{charge}} = |\text{Cl}| + 2|\text{S}|$, apparent sum of anion charges.

Note that $|\text{X}|$ denominates the concentration of element $\langle \text{X} \rangle$ given as atomic (i.e. molar) fraction relative to the sum of all quantified element concentrations with the exclusion of oxygen and lighter elements:

$$|\text{X}_i| = \frac{\langle \text{X}_i \rangle}{\sum \langle \text{X} \rangle} \tag{11}$$

with $|\text{X}_i|$ element concentration index of a particular element with arbitrary index i,

$\sum \langle \text{X} \rangle$ sum of all considered elements (Na, Mg, Al, Si, P, S, Cl, K, Ca, Ti, Cr, Mn, Fe, Co, if not stated differently).

If $r_{cat} > 1$, it is assumed in the upper limit estimate that the excess in the apparent sum of cation charges is produced by the dust contribution. Thus, the dust contribution is calculated as the ion balance excess as

$$c_{dust} = \frac{r_{cat} - 1}{r_{cat}} = \frac{\frac{\sum \text{cations}_{\text{charge}}}{\sum \text{anions}_{\text{charge}}} - 1}{\frac{\text{cations}_{\text{charge}}}{\sum \text{anions}_{\text{charge}}}} = \frac{\sum \text{cations}_{\text{charge}} - \sum \text{anions}_{\text{charge}}}{\sum \text{cations}_{\text{charge}}} \tag{12}$$

Cation excess

If $c_{dust} > 0$, an equal fraction of each element's apparent cation contribution excess is attributed to dust, i.e. the ion charge balance is virtually neutralized for the non-dust component. The dust and non-dust masses are calculated as (see also Table S 2)

$$m_{dust} = \sum \text{dust}_{\text{oxides}} + c_{dust} \sum \text{cations}_{\text{oxide}} \tag{13}$$

with $\sum \text{dust}_{\text{oxides}} = \text{Al}_{\text{oxide}} + \text{Si}_{\text{oxide}} + \text{P}_{\text{oxide}} + \text{Ti}_{\text{oxide}} + \text{Fe}_{\text{oxide}}$,

and $\sum \text{cations}_{\text{oxide}} = \text{Na}_{\text{oxide}} + \text{Mg}_{\text{oxide}} + \text{K}_{\text{oxide}} + \text{Ca}_{\text{carbonate}}$.

Note that stable sulfates (gypsum / anhydrite, alunite) are assigned to the non-dust component.

$$m_{nondust} = (1 - c_{dust}) \sum \text{cations}_{\text{mass}} + \sum \text{anions}_{\text{mass}} \tag{14}$$

with $\sum \text{cations}_{\text{mass}} = \text{Na}_{\text{mass}} + \text{Mg}_{\text{mass}} + \text{K}_{\text{mass}} + \text{Ca}_{\text{mass}}$,

and $\sum \text{anions}_{\text{mass}} = \text{Cl}_{\text{mass}} + \text{SO}^{2-}_{4,\text{mass}}$.

The mass contributions are calculated as shown in Table S 2.

Cation deficit

If $c_{dust} < 0$, i.e. there is a cation deficit, the missing cation is assumed to be ammonium. The dust and non-dust masses are then calculated as

$$m_{dust} = \sum \text{oxides} \tag{15}$$

$$m_{nondust} = \sum \text{cations}_{\text{mass}} + \sum \text{anions}_{\text{mass}} + \text{NH}^{+}_{4,\text{mass}} \tag{16}$$

For calculation of the ammonium mass $\text{NH}^{+}_{4,\text{mass}}$ see Table S 2.

Estimation of the lower limit

The dust mass for lower limit estimate of the dust contribution is calculated according to Eq. (15). The non-dust mass is calculated for $c_{dust} < 0$ according to Eq. (16). For $c_{dust} > 0$ nitrate is assumed to be the missing anion and the non-dust mass is calculated as

$$m_{nondust} = \sum \text{cations}_{\text{mass}} + \sum \text{anions}_{\text{mass}} + \text{NO}^{-}_{3,\text{mass}} \tag{17}$$

Refer to Table S 2 for calculation of the nitrate mass.

Calculation of the dust fraction

From the dust and non-dust mass contributions, the dust volume contribution to the particle is calculated as

$$f_{dust} = \frac{\frac{m_{dust}}{\rho_{dust}}}{\frac{m_{dust}}{\rho_{dust}} + \frac{m_{nondust}}{\rho_{nondust}}} = \frac{m_{dust}}{m_{dust} + \frac{\rho_{dust}}{\rho_{nondust}} m_{nondust}} \tag{18}$$

and the diameter of the resulting dust inclusion as

$$\frac{\pi}{6} d^3_{v,dust} = f_{dust} \frac{\pi}{6} d^3_v \rightarrow \quad d_{v,dust} = f^{\frac{1}{3}}_{dust} d_v \tag{19}$$

S.3 Statistical uncertainty of total volumes / masses and relative number abundances from single particle measurements

When assessing the uncertainty of values based on counted occurrences, frequently the counting statistics are assumed to follow a Poisson distribution. However, when calculating total aerosol masses or volumes, besides the measurement errors in particular the – usually few – large particles can introduce a considerable statistical uncertainty, which is not necessarily accounted for by the distribution assumption. Therefore, estimates of the statistical uncertainty based on single particle counts for an a priori unknown frequency distribution (i. e. the counting frequency distribution modified by the also unknown particle size distribution) either require reasonable assumptions or distribution-independent estimators. In the present work, the uncertainty is estimated by a bootstrap approach with Monte Carlo approximation (Efron 1979).

For the Poisson approach, with a counting error of $\Delta n = 1$ for a single particle count ($n = 1$) the Gaussian error propagation of the standard deviation for a sum of particle volumes V_k resolves to

$$\Delta V = \sqrt{\sum_k \left(\Delta n \frac{\partial}{\partial n} n V_k\right)^2 + \sum_k \left(\Delta V_k \frac{\partial}{\partial V_k} n V_k\right)^2} = \sqrt{\sum_k V_k^2 + \sum_k \Delta V_k^2} \quad (20)$$

with n the number of particles with Volume V_k, in this case always 1,
ΔV_k the volume measurement error,
k the index for the single particles.

Similar considerations apply for the mass calculations.

The two-sided 95 % confidence interval is estimated for the Poisson distribution case as 1.96 times the standard deviation, and for the bootstrap case as the 0.025 to 0.975 quantile range of the bootstrap replications (bias corrected and accelerated method; DiCiccio et al. 1996; Carpenter et al. 2000).

Considering only the statistical uncertainty from Eq. (20), the distribution-based approach can be compared to the bootstrap approach in terms of relative statistical uncertainty for the volume estimated from two methods (Fig. S 1). Clearly, the Poisson assumption underestimates the lower limit of the two-sided 95 % confidence interval (i.e. overestimates the uncertainty), providing even physically meaningless negative numbers. In contrast, the bootstrap approach yields most probably more precise estimates (see also Efron 2003). For the upper limit of the interval, the Poisson approach seems to underestimate the uncertainty, in particular with respect to the high volumes which can be present in single particles (Fig. S 1, left). When restricting the size range to particles of 1 µm to 20 µm in diameter (Fig. S 1, right), as expected the differences in confidence interval limits become much smaller and stay mostly below 20 % difference between the two approaches. Note in particular the impact of the volume in the single largest particle. For the present work, the bootstrap approach is preferred.

For the assessment of the confidence interval of relative counting abundances, frequently a confidence interval based on a binomial distribution is used as estimate (Agresti et al. 1998), i.e. for a relative number abundance of a certain particle type class r the two-sided 95 % confidence interval is approximated as (Hartung et al. 2005)

$$CL_{0.025,0.975} = \frac{3.84 + 2r \mp \sqrt{3.84\left(3.84 + 4r\frac{n-r}{n}\right)}}{2(n+3.84)} \quad (21)$$

with r the count of particles in that class,
n the total number of particles.

The two approaches show much closer agreement here than in the previous case (see Fig. S 2). Note that if the common Wald confidence interval is used (Agresti et al. 1998), with lower absolute particle numbers in a class, an increasing tendency of over/underestimation similar to the previous case occurs up to meaningless negative values in the binomial case. For sake of consistence, in the present work also for the relative abundances the robust bootstrap approach for estimation of the confidence intervals was chosen.

S.4 Determining the size distributions from the free-wing impactor measurements

First, a window correction accounting for the exclusion of particles at the analysis image border is applied (Kandler et al. 2009):

$$c_w = \frac{w_x w_y}{(w_x - d_p)(w_y - d_p)} \quad (22)$$

Second, the collection efficiency of the FWI has to be regarded. Therefore, the ambient particle diameter at the time of collection has to be estimated by accounting for the hygroscopic particle growth:

$$d_{amb} = d_v g_{hyg} \quad (23)$$

with g_{hyg} the hygroscopic growth factor.

Hygroscopic growth can be estimated from the hygroscopicity parameter κ (Petters et al. 2007) as

$$g_{hyg} = \left(1 + \frac{a_w}{1 - a_w}\kappa\right)^{\frac{1}{3}} \quad (24)$$

with a_w the water activity.

As only super-micron particles are considered in this part of the study, the water activity can be equated with the relative humidity given as fraction. The hygroscopicity parameter can be determined as volume-weighted average of the hygroscopicity parameters of the major contributing components (Petters et al. 2007). Assuming a mixture of sodium sulfate and sodium chloride as the components dominating the hygroscopic growth and assigning the dust component zero hygroscopicity, the hygroscopicity parameter is approximated from the volume contributions as

$$\kappa = (1 - f_{dust}) \frac{0.68 \times Na_2SO_{4,volume} + 1.12 \times NaCl_{volume}}{Na_2SO_{4,volume} + NaCl_{volume}} \quad (25)$$

For the calculation of the volume contributions, refer to Table S 2.

The collection efficiency E(P) is parameterized (see below) from the experimentally determined values for discs given by May et al. (1967) as a function of impaction parameter P:

$$P = \frac{S}{D} \quad (26)$$

with S stopping distance,
D characteristic dimension, here 12.5 mm.

While P equals to the Stokes number within the Stokes regime, in the current work the particle Reynolds numbers are considerably higher. In this regime, in analogy to Hinds (1999) the stopping distance can be approximated with better than 3 % accuracy as

$$S=\frac{\rho_{amb} d_{amb}}{\rho_a \sqrt{\chi}}\left[Re_p^{\frac{1}{3}}-\sqrt{6}\tan^{-1}\left(\frac{Re_p^{\frac{1}{3}}}{\sqrt{6}}\right)\right] \quad (27)$$

with ρ_{amb} ambient particle density, estimated from chemical composition and growth factor,
ρ_a air density,
χ aerodynamic shape factor.

Results of the trigonometric function must be given as radian. The dry aerodynamic shape factor is assumed as constant similar to Ott et al. (2008), but is interpolated for particles mixed with water as function of the hygroscopic growth factor:

$$\chi=\begin{cases}1+(\chi_0-1)\left(1-\frac{(g_{hyg}-1)}{(g_{hyg,lim}-1)}\right) & \forall\ g_{hyg}<g_{hyg,lim}\\ 1 & \forall\ g_{hyg}>g_{hyg,lim}\end{cases} \quad (28)$$

with $\chi_0=1.4$ an estimated dry shape factor (Ott et al. 2008)
$g_{hyg,lim}=1.3$ a limiting hygroscopic growth factor starting from which the particles are assumed to be spherical.

The particle Reynolds number is

$$Re_p=\frac{\rho_a v_i d_{amb}}{\eta\sqrt{\chi}} \quad (29)$$

with $v_i=\sqrt{v_r^2+v^2}$ the impaction velocity
$v_r=2\pi l f_r$ the speed of the collector in the plane of rotation
l the collector arm length
f_r the rotation frequency
v the wind speed
η the viscosity of the air.

The stopping distances calculated by Eq. (27) are well in accordance with the parameterization curves shown by May et al. (1967).

The collection E(P) efficiency for P>0.125 is then parameterized (see Fig. S 4) and the according correction is

$$c_e=\frac{1}{E(P)}=\exp\left(\frac{0.28}{P}\right) \quad (30)$$

The total investigated volume for the concentration calculations is determined by

$$V_i=A\ v_i\ t_i \quad (31)$$

with A the analyzed area,
t_i the sample collection time.

The atmospheric concentration is finally

$$C(d_{amb})=\frac{1}{V_i}\sum_k c_w(d_{p,k})c_e(d_{amb,k}) \quad (32)$$

with k index of the particle.

S.5 Determining the airborne size distributions from the sedimentation sampler measurements

Similar to the previous section, sampling efficiency considerations are necessary for the sedimentation sampler. For the supermicron particle size range sedimentation and turbulent impaction dominate the particle deposition velocity. To calculate the turbulent impaction velocity, which depends of the wind speed, the friction velocity is needed. As the opposing inner boundary layers of the sampler plates are always separated for the considered range of wind speeds (boundary layer thickness between 4.5 mm and 2 mm for wind speeds between 3.5 m/s and 13.5 m/s; Munson et al. 2013), the flow inside the sampler is approximated as flow over a smooth flat plate (the lower plate). The friction velocity is calculated as recommended by Wood (1981):

$$u^*=\frac{v}{\sqrt{2}}\left(2\log_{10}Re_s-0.65\right)^{-1.15} \quad (33)$$

with $Re_s=\frac{\rho_a v x}{\eta}$ the flow Reynolds number at the sampling stub location,
x the distance from the lower plate edge to the center of the sampling stub (6.3 cm).

Considering the flow inside the sampler as tube flow (Liu et al. 1974) would lead to friction velocities differing by less than 5 %.

The deposition velocity is estimated by the following formalism, following the approach of Piskunov (2009):

$$v_d=\frac{u^*}{J_1+J_2} \quad (34)$$

$$J_1=\frac{u^*\exp(-1.2\tau^+)}{v_{Stk}}\left[1-\exp\left(-13.204\ Sc^{\frac{2}{3}}\frac{v_{Stk}}{u^*}\right)\right] \quad (35)$$

with $Sc=\frac{\eta}{\rho_a C_D}=\frac{3\pi\eta^2}{\rho_a k_B T}\frac{d_{amb}}{C_c\sqrt{\chi}}$ the Schmidt number,
C_D the particle diffusion coefficient,
k_B the Boltzmann constant,
T the ambient temperature,
$C_c=1+2\frac{\lambda\sqrt{\chi}}{d_{amb}}\left[1.257+0.4\exp\left(-\frac{1.1\ d_{amb}}{2\lambda\sqrt{\chi}}\right)\right]$ the Cunningham slip correction,
$\lambda=\frac{k_B T}{\sqrt{2}\pi d_M^2 P}$ the mean free path,
$d_M=3.68\times10^{-10}$ m the average diameter of an air molecule,
P the ambient pressure,

$$v_{Stk}=\frac{12\,\eta\sqrt{\chi}}{0.42\,C_c\,\rho_a\,d_{amb}}\left[\sqrt{1+\frac{0.42\,C_c^2\,\rho_a\,\rho_{amb}}{108\,\eta^2}\left(\frac{d_{amb}}{\sqrt{\chi}}\right)^3\left(1-\frac{\rho_a}{\rho_{amb}}\right)g}-1\right]$$

the gravitational settling velocity,

g the gravitational acceleration;

$$J_2=\frac{1-\exp\left[-\gamma\left(1+\frac{v_{Stk}}{u^*\,p_\tau}\right)\right]}{p_\tau+\frac{v_{Stk}}{u^*}} \quad (36)$$

with $\gamma=\frac{0.4611\,Sc\,\tau^+(1+0.3859\,\tau^+)}{(1+0.1193\,\tau^+)(1+0.1193\,\tau^++6.613\,Sc)}$

$\tau^+=\frac{u^{*2}}{\eta}\frac{\rho_a}{g}v_{Stk}$ the dimensionless relaxation time,

$p_\tau=\frac{\tau^+(1+0.3859\,\tau^+)}{65.06\,(1+0.1193\,\tau^+)^2}$

The atmospheric concentrations are then

$$C(d_{amb})=\frac{1}{A\,t_i}\sum_k\frac{c_w(d_{p,k})}{v_d(d_{amb,k})} \quad (37)$$

A major bias for this calculation originates from the uncertainty in (turbulent) deposition velocity.

The aerodynamic diameter used here is calculated as:

$$d_a=\sqrt{\frac{\rho_{amb}}{\rho_0\chi}}\,d_{amb} \quad (38)$$

with $\rho_0=1000\frac{kg}{m^3}$ unity density.

References

Agresti, A., B. A. Coull (1998): Approximate Is Better than "Exact" for Interval Estimation of Binomial Proportions. Am. Stat. 52(2), 119-126. doi: 10.2307/2685469

Carpenter, J., J. Bithell (2000): Bootstrap confidence intervals: when, which, what? A practical guide for medical statisticians. Stat. Med. 19(9), 1141-1164. doi: 10.1002/(sici)1097-0258(20000515)19:9<1141::aid-sim479>3.0.co;2-f

Deer, W. A., R. A. Howie, J. Zussman (1992): An Introduction to the Rock-Forming Minerals. Second Edition. Harlow, UK, Pearson Education Ltd.

DiCiccio, T. J., B. Efron (1996): Bootstrap confidence intervals. Statist. Sci. 11(3), 189-228. doi: 10.1214/ss/1032280214

Efron, B. (1979): Bootstrap Methods: Another Look at the Jackknife. Ann. Statist.(1), 1-26. doi: 10.1214/aos/1176344552

Efron, B. (2003): Second Thoughts on the Bootstrap. Statist. Sci. 18(2), 135-140. doi: 10.1214/ss/1063994968

Hartung, J., B. Elpelt, K.-H. Klösener (2005): Statistik: Lehr- und Handbuch der angewandten Statistik., Oldenbourg, Munich, Germany.

Hinds, W. C. (1999): Aerosol Technology. Properties, behavior, and measurement of airborne particles. Second edition. New York, USA, Wiley Interscience.

Kandler, K., L. Schütz, C. Deutscher, H. Hofmann, S. Jäckel, P. Knippertz, K. Lieke, A. Massling, A. Schladitz, B. Weinzierl, S. Zorn, M. Ebert, R. Jaenicke, A. Petzold, S. Weinbruch (2009): Size distribution, mass concentration, chemical and mineralogical composition, and derived optical parameters of the boundary layer aerosol at Tinfou, Morocco, during SAMUM 2006. Tellus 61B, 32-50. doi: 10.1111/j.1600-0889.2008.00385.x

Kristensen, T. B., T. Müller, K. Kandler, N. Benker, M. Hartmann, J. M. Prospero, A. Wiedensohler, F. Stratmann (2016): Properties of cloud condensation nuclei (CCN) in the trade wind marine boundary layer of the western North Atlantic. Atmos. Chem. Phys. 16(4), 2675-2688. doi: 10.5194/acp-16-2675-2016

Liu, B. Y. H., J. K. Agarwal (1974): Experimental observation of aerosol deposition in turbulent flow. J. Aerosol Sci. 5(2), 145-155. doi: 10.1016/0021-8502(74)90046-9

May, K. R., R. Clifford (1967): The impaction of aerosol particles on cylinders, spheres, ribbons and discs. Ann. Occup. Hyg. 10, 83-95.

Munson, B. R., T. H. Okiishi, W. W. Huebsch, A. P. Rothmayer (2013): Fundamentals of Fluid Mechanics, 7th Edition, John Wiley & Sons.

Ott, D. K., W. Cyrs, T. M. Peters (2008): Passive measurement of coarse particulate matter, $PM_{10-2.5}$. J. Aerosol Sci. 39(2), 156-167. doi: 10.1016/j.jaerosci.2007.11.002

Petters, M. D., S. M. Kreidenweis (2007): A single parameter representation of hygroscopic growth and cloud condensation nucleus activity. Atmos. Chem. Phys. 7(8), 1961-1971. doi: 10.5194/acp-7-1961-2007

Piskunov, V. N. (2009): Parameterization of aerosol dry deposition velocities onto smooth and rough surfaces. J. Aerosol Sci. 40(8), 664-679. doi: 10.1016/j.jaerosci.2009.04.006

Warneck, P., J. Williams (2012): The Atmospheric Chemist's Companion. Numerical Data for Use in the Atmospheric Sciences, Springer Netherlands.

Wood, N. B. (1981): A simple method for the calculation of turbulent deposition to smooth and rough surfaces. J. Aerosol Sci. 12(3), 275-290. doi: 10.1016/0021-8502(81)90127-0

Table S 1: Sample denominations and collection times for the campaigns in 2013 and 2016.

2013									*2016*		
DPDS sample	**starting time (UTC), year-month-day hour:minute**	**duration, hours:minutes**	**FWI sample**	**starting time (UTC), year-month-day hour:minute**	**duration, hours:minutes**	**CI sample**	**starting time (UTC), year-month-day hour:minute**	**duration, hours:minutes**	**DPDS sample**	**starting time (UTC), year-month-day hour:minute**	**duration, hours:minutes**
RPS_001	2013-06-14 21:19	19:06	RPF_01	2013-06-15 15:48	0:30	RPE_01	2013-06-15 15:50	0:10	RPS_031	2016-08-06 20:50	17:15
RPS_002	2013-06-15 16:25	20:41							RPS_032	2016-08-07 14:10	26:10
RPS_003	2013-06-16 13:08	25:29	RPF_02	2013-06-16 13:16	0:30	RPE_02	2013-06-16 13:20	0:10	RPS_033	2016-08-08 16:20	21:32
RPS_004	2013-06-17 14:39	23:09	RPF_03	2013-06-17 14:42	0:30	RPE_03	2013-06-17 14:55	0:10	RPS_034	2016-08-09 13:52	23:58
RPS_005	2013-06-18 13:49	23:15	RPF_04	2013-06-18 13:50	0:30	RPE_04	2013-06-18 14:00	0:06	RPS_035	2016-08-10 13:50	25:48
RPS_006	2013-06-19 13:04	24:23	RPF_05	2013-06-19 13:12	0:30	RPE_05	2013-06-19 13:15	0:10	RPS_036	2016-08-11 15:38	2:43
RPS_007	2013-06-20 13:27	28:19	RPF_06	2013-06-20 13:37	0:30	RPE_06	2013-06-20 13:40	0:20	RPS_037	2016-08-11 18:21	19:26
RPS_008	2013-06-21 17:46	25:16	RPF_07	2013-06-21 18:20	1:00	RPE_07	2013-06-21 18:10	0:20	RPS_038	2016-08-12 13:47	23:30
RPS_009	2013-06-22 19:02	42:08	RPF_08	2013-06-22 19:05	0:30	RPE_08	2013-06-22 19:20	0:20	RPS_039	2016-08-13 13:17	23:54
RPS_010	2013-06-24 13:10	24:13	RPF_09	2013-06-24 13:14	1:30	RPE_09	2013-06-24 13:20	0:40	RPS_040	2016-08-14 13:11	23:23
RPS_011	2013-06-25 13:23	23:32	RPF_10	2013-06-25 14:27	1:47	RPE_10	2013-06-25 14:30	1:00	RPS_041	2016-08-15 12:34	24:26
RPS_013	2013-06-26 12:55	24:21	RPF_11	2013-06-26 12:58	1:00	RPE_11	2013-06-26 13:00	0:30	RPS_042	2016-08-16 13:00	27:35
			RPF_12	2013-06-27 02:43	1:00	RPE_12	2013-06-27 02:30	0:30	RPS_043	2016-08-17 16:35	22:05
RPS_014	2013-06-27 13:16	24:10	RPF_13	2013-06-27 13:20	0:20	RPE_13	2013-06-27 13:30	0:30	RPS_044	2016-08-18 14:40	21:06
			RPF_13B	2013-06-27 15:49	1:15				RPS_045	2016-08-19 11:46	26:08
RPS_015	2013-06-28 13:26	23:43	RPF_14	2013-06-28 13:38	1:00	RPE_14	2013-06-28 13:45	0:30	RPS_046	2016-08-20 13:54	22:15
RPS_016	2013-06-29 13:09	24:17				RPE_15	2013-06-29 13:10	0:48	RPS_047	2016-08-21 12:09	24:41
RPS_017	2013-06-30 13:26	23:39	RPF_16	2013-06-30 15:47	0:30	RPE_16	2013-06-30 13:35	0:15	RPS_048	2016-08-22 12:50	23:47
RPS_018	2013-07-01 13:05	23:20	RPF_17	2013-07-01 13:11	1:00	RPE_17	2013-07-01 13:20	0:20	RPS_049	2016-08-23 12:37	23:32
RPS_019	2013-07-02 12:25	23:28	RPF_18	2013-07-02 12:31	1:13	RPE_18	2013-07-02 12:25	0:40	RPS_050	2016-08-24 12:09	23:54
RPS_020	2013-07-03 11:53	25:43	RPF_19	2013-07-03 11:58	1:08	RPE_19	2013-07-03 11:55	0:45	RPS_051	2016-08-25 12:03	23:37
RPS_021	2013-07-04 13:36	23:20	RPF_20	2013-07-04 13:43	0:30	RPE_20	2013-07-04 13:35	0:30	RPS_052	2016-08-26 11:40	23:16
RPS_022	2013-07-05 12:56	23:22	RPF_21	2013-07-05 13:01	1:00	RPE_21	2013-07-05 13:00	0:40			
RPS_023	2013-07-06 12:18	25:52	RPF_22	2013-07-06 12:16	1:20	RPE_22	2013-07-06 12:14	0:45			
RPS_024	2013-07-07 14:10	24:16	RPF_23	2013-07-07 14:20	1:00	RPE_23	2013-07-07 14:15	1:00			
RPS_025	2013-07-08 14:26	47:40	RPF_24	2013-07-08 17:15	0:30	RPE_24	2013-07-08 17:30	0:25			
RPS_026	2013-07-10 14:06	22:45	RPF_25	2013-07-10 15:00	0:30	RPE_25	2013-07-10 15:00	0:15			
RPS_027	2013-07-11 12:51	22:26	RPF_26	2013-07-11 12:57	0:23	RPE_26	2013-07-11 13:00	0:15			
RPS_028	2013-07-12 11:17	25:56	RPF_27	2013-07-12 11:17	0:30	RPE_27	2013-07-12 11:24	0:20			
RPS_029	2013-07-13 13:13	24:00	RPF_28	2013-07-13 13:19	1:00	RPE_28	2013-07-13 13:15	0:40			
RPS_030	2013-07-14 13:13	23:40	RPF_29	2013-07-14 13:18	1:52	RPE_29	2013-07-14 13:20	0:50			
			RPF_30	2013-07-15 12:58	1:30	RPE_30	2013-07-15 13:00	0:40			

Table S 2: Conversion formulas used for the calculation of oxide, carbonate, element atomic and ammonium masses, as well as sodium sulfate and sodium chloride volumes. Values were taken from Deer et al. (1992) and Warneck et al. (2012).

$Al_{oxide}=101.96\ \frac{g}{mol}\times\frac{\lvert Al\rvert}{2}$	$Na_{oxide}=61.98\ \frac{g}{mol}\times\frac{\lvert Na\rvert}{2}$
$Si_{oxide}=60.08\ \frac{g}{mol}\times\lvert Si\rvert$	$Mg_{oxide}=40.30\ \frac{g}{mol}\times\lvert Mg\rvert$
$P_{oxide}=141.94\ \frac{g}{mol}\times\frac{\lvert P\rvert}{2}$	$K_{oxide}=94.20\ \frac{g}{mol}\times\frac{\lvert K\rvert}{2}$
$Ti_{oxide}=79.88\ \frac{g}{mol}\times\lvert Ti\rvert$	$Ca_{carbonate}=100.09\ \frac{g}{mol}\times\lvert Ca\rvert$
$Fe_{oxide}=159.69\ \frac{g}{mol}\times\frac{\lvert Fe\rvert}{2}$	
$Na_{mass}=22.99\ \frac{g}{mol}\times\lvert Na\rvert$	$Cl_{mass}=35.45\ \frac{g}{mol}\times\lvert Cl\rvert$
$Mg_{mass}=24.31\ \frac{g}{mol}\times\lvert Mg\rvert$	$SO_{4,mass}=96.06\ \frac{g}{mol}\times\lvert S\rvert$
$K_{mass}=39.10\ \frac{g}{mol}\times\lvert K\rvert$	$NH_{4,mass}=-18.04\ \frac{g}{mol}\times c_{dust}$
$Ca_{mass}=40.08\ \frac{g}{mol}\times\lvert Ca\rvert$	$NO_{3,mass}=62.00\ \frac{g}{mol}\times c_{dust}$
$Na_2SO_{4,volume}=\frac{142.04\frac{g}{mol}\times\lvert X\rvert}{2.66\frac{g}{cm^3}}$ $\begin{cases}X=Na, & \text{if classified as insoluble sulfate}\\ X=S & \text{in other cases}\end{cases}$	
$NaCl_{volume}=\frac{58.44\frac{g}{mol}\times\lvert Cl\rvert}{2.17\frac{g}{cm^3}}$	

Table S 3: Relationships between area coverage of the simulated 5 mm x 5 mm analysis field, particle numbers, particle masses and uncertainties. Upper part: CV-ground size distribution, lower part: CV-air size distribution. A bulk density of 2500 kg/m³ was assumed for the mass estimation from particle volume. Abbreviations: SP coverage = ratio of the sum of single particle cross sections to the analysis field; apparent coverage = fraction of area covered by the particles after deposition; $N_{>1}$ = Number of particles larger than 1 µm diameter; $PM_{>1}$ = Total mass of particles larger than 1 µm diameter (approx. 99.99 % of total mass); $PM_{1\text{-}32}$ = total mass of particles between 1 µm and 32 µm diameter (approx. 50 % of total mass for source-near size distribution, 67 % for aged one). Relative uncertainty is given as the ratio of the upper and lower bounds of the central 95 % quantile to the median of 1000 (200 for SP coverage >= 0.1) repetitions of deposition simulation.

SP coverage	Apparent coverage	$N_{>1}$	$PM_{>1}$, µg	relative uncertainty	$PM_{1\text{-}32}$, µg	relative uncertainty
0.001	0.001	353	0.8	0.38 - 4.16	0.5	0.56 - 1.38
0.003	0.002	865	2.7	0.37 - 4.68	1.3	0.69 - 1.24
0.005	0.005	1699	4.6	0.53 - 3.60	2.5	0.78 - 1.18
0.006	0.006	2032	6.1	0.49 - 2.80	3.0	0.81 - 1.17
0.007	0.007	2361	6.9	0.54 - 2.76	3.5	0.82 - 1.16
0.008	0.008	2692	7.6	0.56 - 2.59	4.0	0.83 - 1.14
0.009	0.009	3016	8.3	0.58 - 2.57	4.5	0.84 - 1.14
0.010	0.010	3344	10	0.54 - 2.21	5.0	0.85 - 1.13
0.011	0.011	3669	11	0.57 - 2.26	5.5	0.85 - 1.13
0.012	0.012	3988	11	0.63 - 2.18	5.9	0.86 - 1.12
0.013	0.013	4313	13	0.64 - 2.03	6.4	0.87 - 1.12
0.015	0.015	4951	14	0.67 - 1.95	7.4	0.88 - 1.11
0.020	0.020	6520	20	0.69 - 2.09	9.8	0.89 - 1.10
0.025	0.025	8047	24	0.74 - 1.94	12	0.90 - 1.09
0.035	0.034	10998	34	0.77 - 1.71	17	0.92 - 1.07
0.050	0.048	15146	56	0.69 - 1.48	24	0.93 - 1.06
0.075	0.071	21379	81	0.75 - 1.45	36	0.94 - 1.05
0.100	0.093	26824	106	0.79 - 1.35	47	0.95 - 1.05
0.200	0.172	34099	218	0.80 - 1.53	89	0.97 - 1.04
0.001	0.001	1031	0.7	0.44 - 3.05	0.5	0.66 - 1.33
0.005	0.005	5056	3.6	0.73 - 1.84	2.4	0.84 - 1.15
0.010	0.010	9990	8.1	0.71 - 1.42	4.8	0.89 - 1.11
0.025	0.025	24102	19.8	0.79 - 1.27	11.9	0.93 - 1.07
0.050	0.048	45618	39.4	0.82 - 1.38	23.4	0.95 - 1.05
0.075	0.071	64665	59.1	0.85 - 1.29	34.6	0.96 - 1.04
0.100	0.093	81568	78.5	0.89 - 1.23	45.4	0.97 - 1.04
0.150	0.134	109224	118	0.90 - 1.17	65.7	0.97 - 1.03
0.200	0.173	129769	158	0.91 - 1.13	84.2	0.97 - 1.02

Table S 4: 95 % quantile of the fractions of internally mixed particles due to coincidental mixture on the substrate, for a two-component system with CV-ground size distribution. Strong mixture refers to a minimum particle volume fraction of the other component of 20 %, detectable mixture refers to 1 %. Only values larger than 0.001 are shown, values larger than 0.05 are highlighted in bold.

strong mixture		size range, µm						
component ratio	apparent area coverage	>1-2	>2-4	>4-8	>8-16	>16-32	>32-64	>64-128
50 % / 50 %	0.001				.007			
	0.005			.002	.007	.027		
	0.010			.002	.010	.032	.042	
	0.025		.001	.003	.018	**.051**	.038	
	0.048		.001	.004	.032	**.084**	.044	**.077**
	0.071		.001	.006	.045	**.116**	**.053**	**.077**
	0.093		.002	.007	**.057**	**.145**	**.064**	**.086**
	0.172	.001	.002	.012	**.102**	**.254**	**.121**	**.108**
90 % / 10 %	0.001							
	0.005			.002	.003	.014		
	0.010				.004	.018		
	0.025		.001	.001	.007	.023	.024	
	0.048			.002	.012	.034	.023	**.059**
	0.071			.002	.017	.045	.025	**.050**
	0.093			.003	.021	**.055**	.031	.040
	0.172		.001	.005	.037	**.091**	.046	**.051**
99 % / 1 %	0.001							
	0.005				.001			
	0.010					.006		
	0.025				.001	.005		
	0.048				.002	.006	.010	
	0.071				.002	.007	.008	
	0.093				.003	.008	.006	
	0.172				.005	.011	.008	.016

detectable mixture		size range, µm						
component ratio	apparent area coverage	>1-2	>2-4	>4-8	>8-16	>16-32	>32-64	>64-128
50 % / 50 %	0.001				.008	.043		
	0.005			.003	.011	**.050**	**.167**	
	0.010		.003	.003	.015	**.071**	**.158**	**.250**
	0.025		.002	.005	.029	**.125**	**.214**	**.286**
	0.048		.003	.008	**.054**	**.206**	**.327**	**.333**
	0.071	.001	.003	.011	**.077**	**.284**	**.427**	**.409**
	0.093	.001	.004	.014	**.098**	**.354**	**.526**	**.500**
	0.172	.002	.007	.025	**.176**	**.563**	**.777**	**.836**
90 % / 10 %	0.001							
	0.005			.002	.005	.027	**.100**	
	0.010			.002	.007	.034	**.083**	
	0.025		.001	.002	.012	**.051**	**.104**	**.167**
	0.048		.001	.003	.020	**.083**	**.146**	**.182**
	0.071		.002	.004	.029	**.110**	**.178**	**.200**
	0.093		.002	.005	.037	**.133**	**.210**	**.217**
	0.172		.003	.010	**.065**	**.221**	**.331**	**.294**
99 % / 1 %	0.001							
	0.005				.002			
	0.010				.002	.007		
	0.025				.002	.010	.026	
	0.048				.003	.013	.029	.067
	0.071				.004	.015	.033	.056
	0.093				.005	.018	.035	.049
	0.172			.001	.008	.027	**.050**	**.053**

Table S 5: 95 % quantile of the fractions of internally mixed particles due to coincidental mixture on the substrate, for a two-component system with CV-air size distribution. Strong mixture refers to a minimum particle volume fraction of the other component of 20 %, detectable mixture refers to 1 %. Only values larger than 0.001 are shown, values larger than 0.05 are highlighted in bold.

strong mixture		size range, µm						
component ratio	**apparent area coverage**	**>1-2**	**>2-4**	**>4-8**	**>8-16**	**>16-32**	**>32-64**	**>64-128**
50 % / 50 %	0.001			.005				
	0.005		.001	.004	.007	.014		
	0.010		.002	.005	.009	.020	.053	
	0.025		.003	.010	.016	.032	.049	
	0.048		.005	.017	.027	**.052**	**.059**	
	0.093	.002	.010	.032	.049	**.090**	**.090**	**.154**
	0.134	.002	.014	.046	**.070**	**.128**	**.127**	**.167**
	0.173	.003	.019	**.060**	**.092**	**.166**	**.163**	**.176**
90 % / 10 %	0.001							
	0.005			.002	.003	.012		
	0.010			.002	.004	.011		
	0.025		.001	.004	.007	.014	.024	
	0.048		.002	.007	.011	.021	.031	
	0.093		.004	.012	.019	.034	.039	**.111**
	0.134		.005	.017	.027	.049	**.053**	**.091**
	0.173	.001	.007	.022	.034	**.061**	**.063**	**.095**
99 % / 1 %	0.001							
	0.005							
	0.010				.001			
	0.025				.002	.002		
	0.048			.001	.002	.004	.010	
	0.093			.002	.003	.005	.009	
	0.134			.002	.003	.007	.012	
	0.173			.003	.004	.008	.011	**.053**

detectable mixture		size range, µm						
component ratio	**apparent area coverage**	**>1-2**	**>2-4**	**>4-8**	**>8-16**	**>16-32**	**>32-64**	**>64-128**
50 % / 50 %	0.001		.002	.005	.013	**.050**		
	0.005		.002	.008	.020	.043	**.125**	
	0.010		.003	.012	.029	**.059**	**.143**	
	0.025	.001	.006	.024	**.059**	**.106**	**.186**	**.500**
	0.048	.002	.010	.045	**.108**	**.188**	**.278**	**.521**
	0.093	.003	.019	**.085**	**.199**	**.329**	**.453**	**.667**
	0.134	.004	.028	**.121**	**.278**	**.453**	**.599**	**.750**
	0.173	.006	.037	**.156**	**.352**	**.556**	**.714**	**.864**
90 % / 10 %	0.001			.005	.011			
	0.005		.001	.004	.009	.022	**.071**	
	0.010		.001	.005	.013	.027	**.071**	
	0.025		.002	.010	.024	.045	**.093**	**.333**
	0.048		.004	.017	.041	**.073**	**.124**	**.333**
	0.093	.001	.007	.031	**.073**	**.126**	**.185**	**.333**
	0.134	.002	.010	.045	**.104**	**.171**	**.236**	**.400**
	0.173	.002	.014	**.057**	**.131**	**.213**	**.287**	**.409**
99 % / 1 %	0.001							
	0.005			.001	.003	.011		
	0.010			.001	.003	.006		
	0.025			.002	.004	.009	.023	
	0.048			.002	.006	.012	.027	
	0.093			.004	.009	.017	.029	**.111**
	0.134		.001	.005	.013	.022	.036	**.111**
	0.173		.002	.007	.016	.027	.044	**.111**

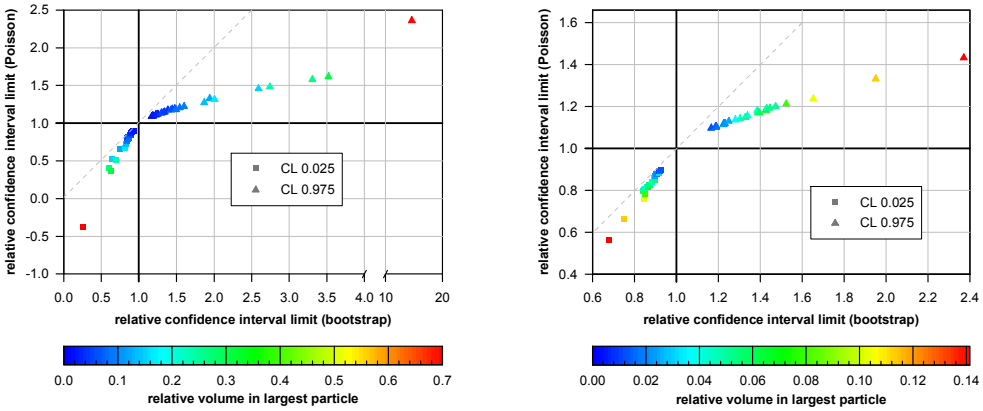

Fig. S 1: Comparison of the relative two-sided 95 % confidence interval limits for bootstrap and Poisson approaches. Values shown are the confidence interval limits for the total deposited particle volume divided by this volume. Data basis are the deposition samples at Ragged Point of 2013. Left: for all particles; right: for particles between 1 µm and 20 µm diameter. The color shows the fraction of the total volume present in the single largest particle. Note the different scales between the graphs.

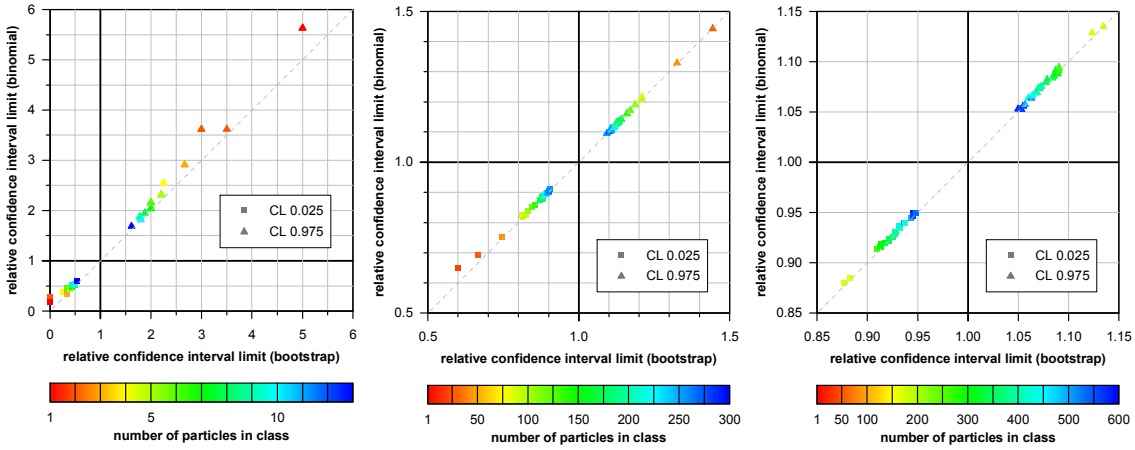

Fig. S 2: Comparison of two-sided 95 % confidence interval limits relative to the relative number abundance of a particle type class. Data basis are the deposition samples at Ragged Point. a: for a low-abundance class (0–1.2 % relative number abundance); b: for a medium-abundance class (2.4–41.8 %); c: for a high-abundance class (27.5–61.9 %). The color shows the absolute number of particles in the according class. Note the different scales between the graphs.

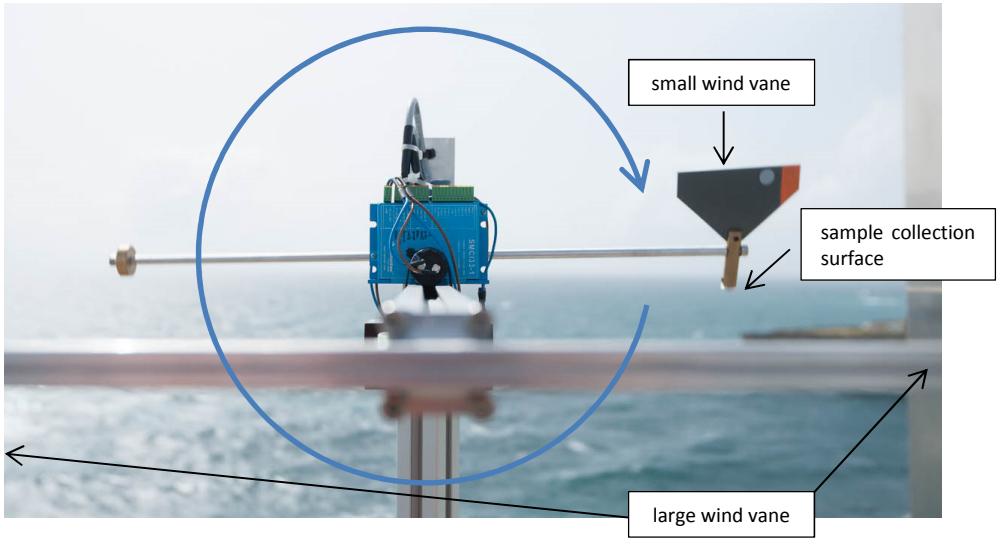

Fig. S 3: Free-wing impactor during rotation (indicated by the blue arc) depicted with 1.25 × 10^{-5} s exposure time. Wind is blowing towards the observer. Note the inclined orientation of the sampling substrate on the right relative to the rotation plane, aligned with the sum vector of wind and rotation movement.

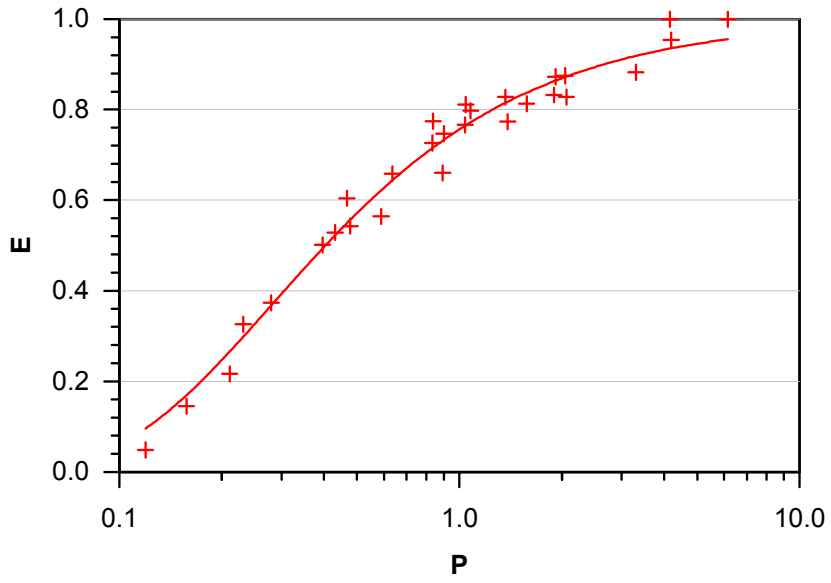

Fig. S 4: Parameterization of collection efficiency E of a disc as function of impaction parameter P; fit to the data of May et al. (1967). Fit function is shown as continuous line.

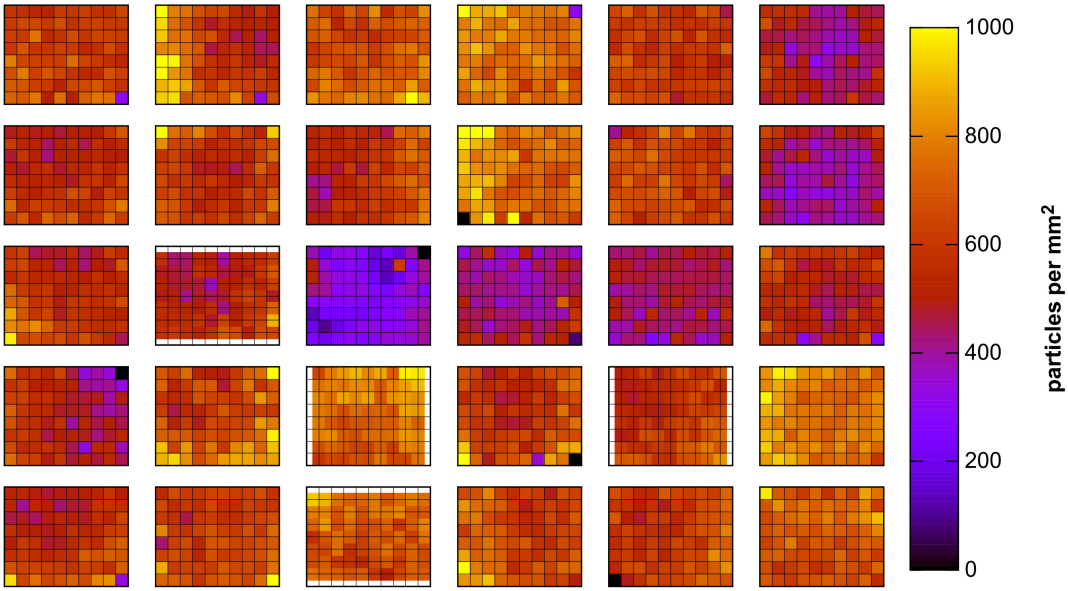

Fig. S 5: Maps of particle deposition density on the FWI substrates for 4 µm < d_g < 8 µm. Each division on the x and y axes equals 1 mm distance.

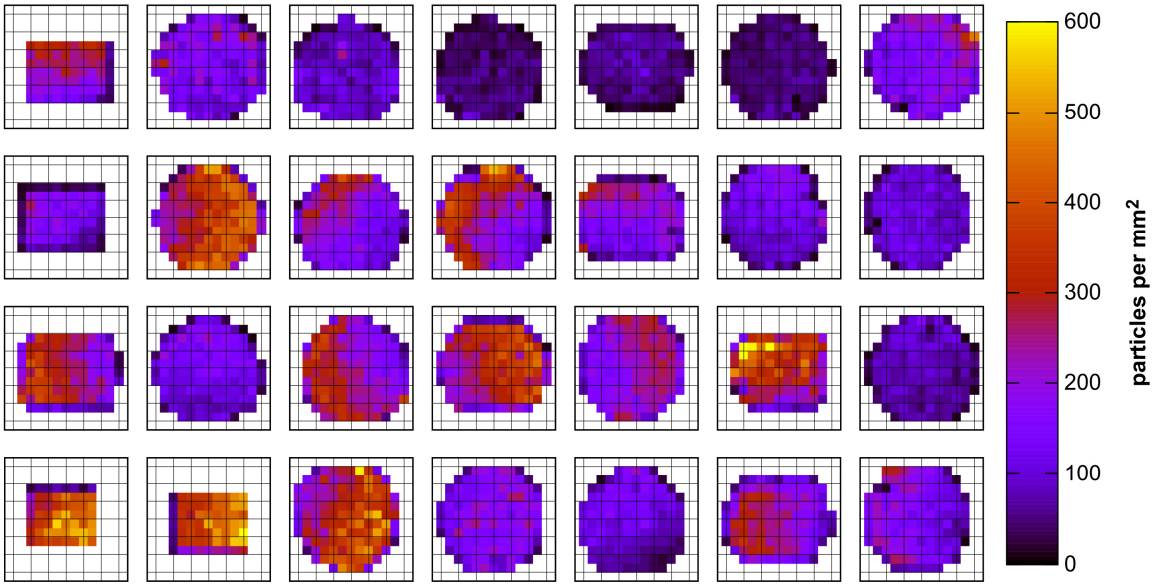

Fig. S 6: Maps of particle deposition density on the DPDS substrates for 4 µm < d_g < 8 µm. Each division on the x and y axes equals 2 mm distance.

Detectable mixture: CV-ground

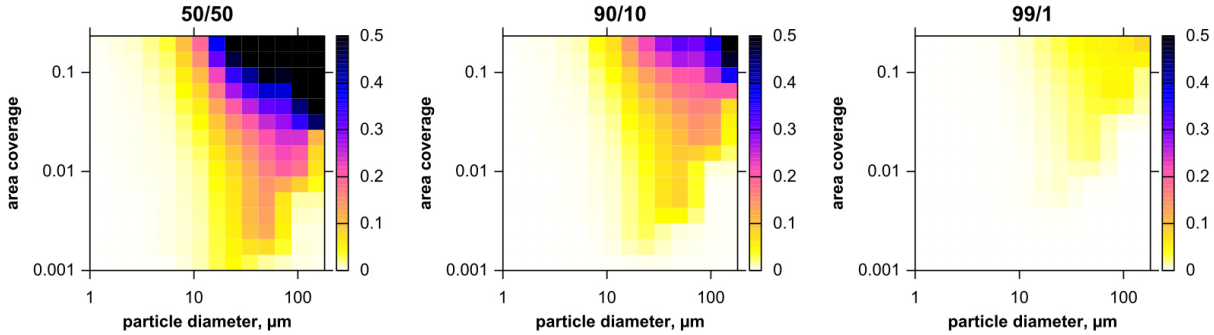

Detectable mixture: CV-air

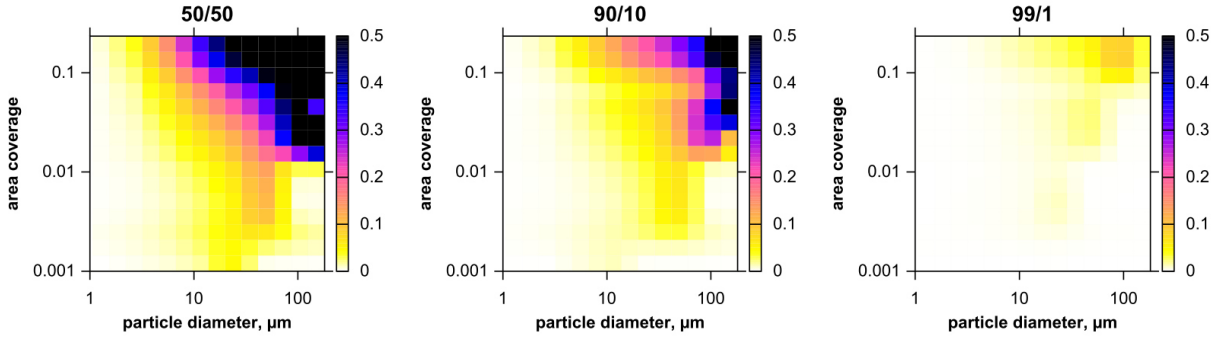

Strong mixture: CV-ground

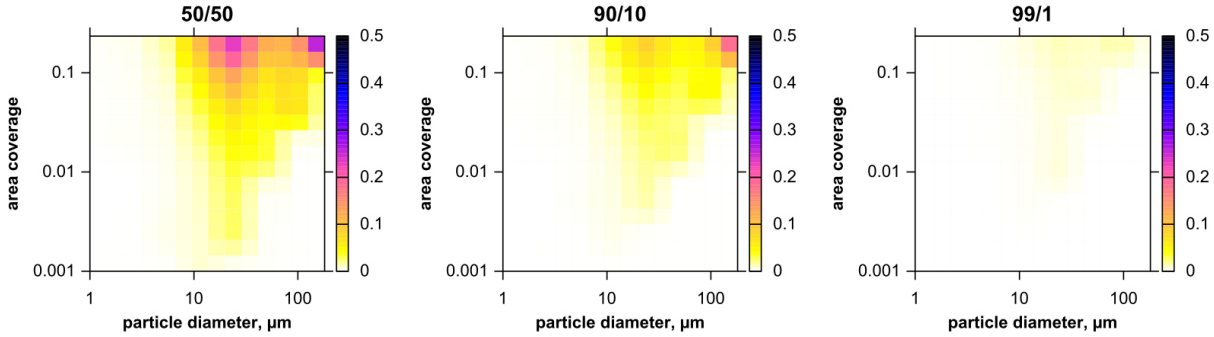

Strong mixture: CV-air

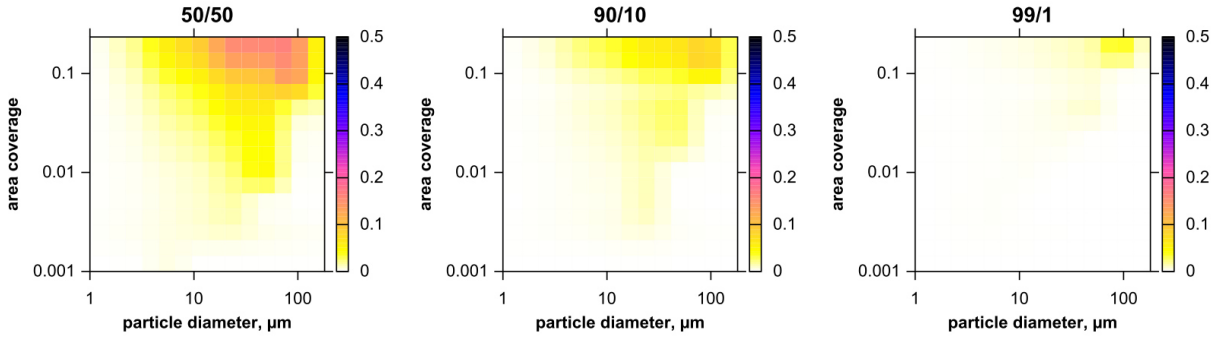

Fig. S 7: Upper 95 % quantile of the fractions of internally mixed particles due to coincidental mixture on the substrate (color scale) as function of the projected area diameter and substrate area coverage, for a two-component system. Strong mixture refers to a minimum particle volume fraction of the other component of 20 %, detectable mixture refers to 1 %. Ratios of the two components in the base aerosol are given as percentages above each plot.

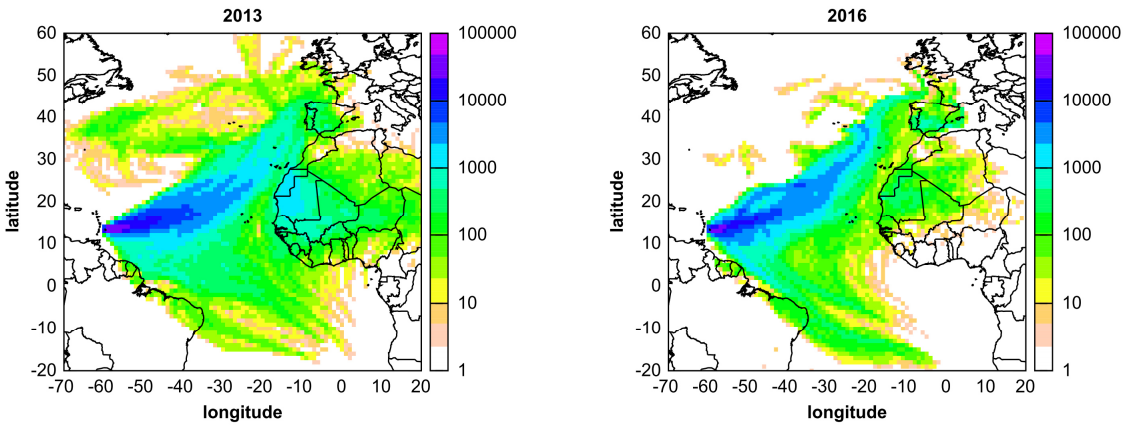

Fig. S 8: Potential air mass provenance during the measurement campaigns 2013 and 2016. A location is counted as potential provenance, if the trajectory at this point is lower than modeled boundary layer height. Colors indicate number of according trajectory point for each grid cell, corrected for differences in grid cell area.

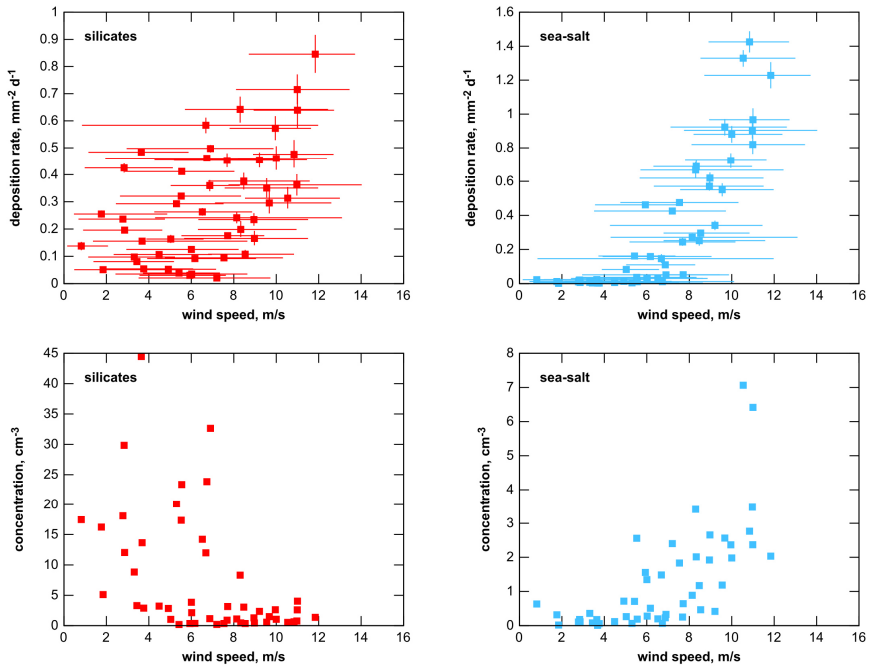

Fig. S 9: Total number deposition rate (upper graphs) and total number concentrations calculated with the Piskunov model (lower graphs) for all samples of 2013 and 2016 as function of wind speed for silicate and sea-salt particles. In the upper graphs, variation in wind speed is given as central 95 % quantile of 1-minute averages, and statistical uncertainty of the deposition rate is shown as two-sided 95 % confidence interval.

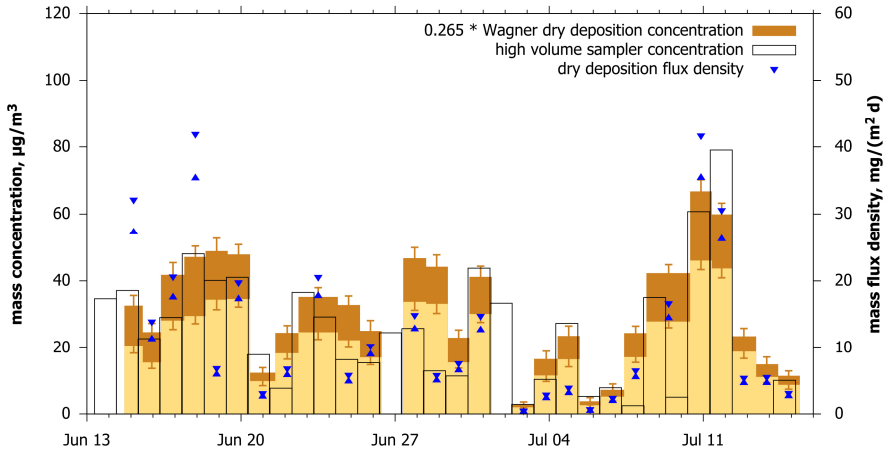

Fig. S 10: Dust mass concentration and flux density time series derived from DPDS data with a linearly tuned Wagner deposition velocity model, compared to such obtained from the a high-volume sampler (Kristensen et al. 2016). The darker brown bar shows the range from lower to upper estimate, the blue triangles the lower and upper estimate of dust deposition flux density.

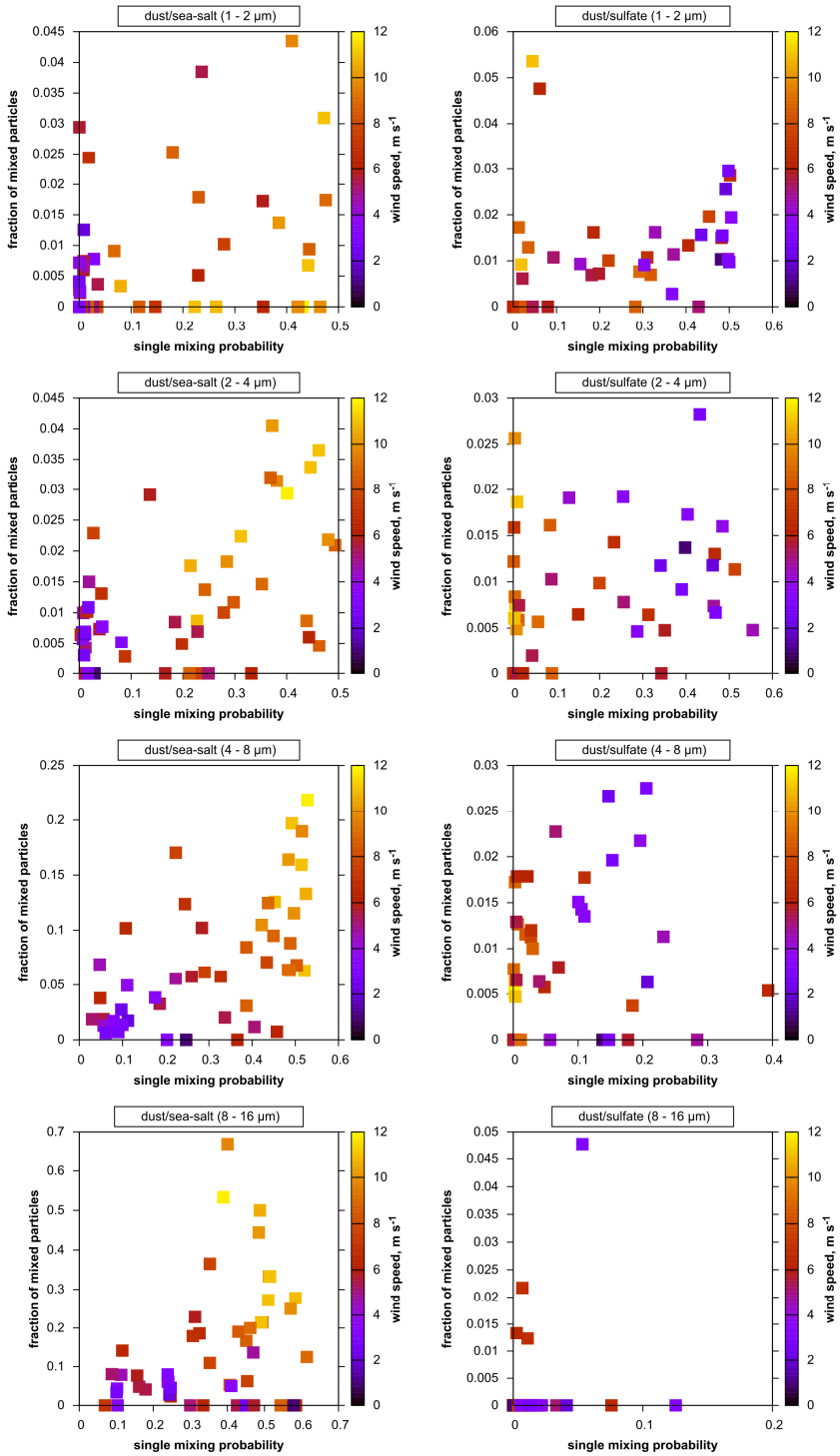

Fig. S 11: Ratio of binary mixed particle abundance to according pure compound abundance as function of the size-restricted single mixing probability. Deposition rate is color coded.